Impact of Voltage Polarity on Time-Dependent Dielectric Breakdown of 1-nm MgO-Based STT-MRAM With Self-Heating Correction

Joel Tan, *Graduate Student Member, IEEE*, Jia Hao Lim, Bejoy Sikder, *Graduate Student Member, IEEE*, Md. Zunaid Baten, *Senior Member, IEEE*, Jae Hyun Kwon, Kazutaka Yamane, Vinayak Bharat Naik, Nagarajan Raghavan, *Member, IEEE*, and Kin Leong Pey, *Senior Member, IEEE*

***Abstract*— Time-dependent dielectric breakdown (TDDB) lifetime of ultrathin (1 nm) MgO in spin-transfer torque magnetoresistive random access memory (STT-MRAM) devices has recently been shown to be driven by factors other than voltage alone. This study focuses on the specific role of asymmetry in the current flow for different polarity pulsing modes of voltage stress on the TDDB lifetime of 1-nm MgO. Numerical analysis, based on a 3-D heat-diffusion equation and spintronic simulations, has been performed to characterize the temperature rise in the devices for precise correction of self-heating to obtain a correct interpretation of MgO TDDB. It is shown that the different lifetimes for the positive and negative modes can be attributed to different temperature increases arising from self-heating. While the positive and negative modes displayed a non-Arrhenius behavior, the bipolar mode showed an Arrhenius trend in which we observed a unique bimodal behavior of TDDB activation energy (E_a) as a function of stress voltage in the ultrathin MgO stack. We discuss the role of additional driving forces, such as current, self-heating, charge trapping, and interface strain governing the breakdown mechanism along with the voltage effect.**

***Index Terms*— Activation energy, Arrhenius, polarity dependence, self-heating, spin-transfer torque magnetoresistive random access memory (STT-MRAM), time-dependent dielectric breakdown (TDDB).**

Manuscript received 7 October 2022; accepted 4 November 2022. Date of publication 14 November 2022; date of current version 3 January 2023. This work was supported by the Economic Development Board (EDB), Singapore University of Technology and Design (SUTD) through the Industry Postgraduate Program (IPP) on STT-MRAM Devices with GlobalFoundries under Project IGIPGF2001. The work of Nagarajan Raghavan was supported by the A*STAR BRENAIC Research Project for Open Access publication under Grant A18A5b0056. The review of this article was arranged by Editor J. Kang. *(Corresponding author: Joel Tan.)*

Joel Tan is with the Engineering Product Development (EPD) Pillar, Singapore University of Technology and Design (SUTD), Singapore 487372, and also with GlobalFoundries, Singapore 738406 (e-mail: joeltan@mymail.sutd.edu.sg).

Jia Hao Lim, Jae Hyun Kwon, Kazutaka Yamane, and Vinayak Bharat Naik are with GlobalFoundries, Singapore 738406.

Bejoy Sikder and Md. Zunaid Baten are with the Department of Electrical and Electronic Engineering (EEE), Bangladesh University of Engineering and Technology (BUET), Dhaka 1205, Bangladesh.

Nagarajan Raghavan and Kin Leong Pey are with the Engineering Product Development (EPD) Pillar, Singapore University of Technology and Design (SUTD), Singapore 487372.

Color versions of one or more figures in this article are available at https://doi.org/10.1109/TED.2022.3220485.

Digital Object Identifier 10.1109/TED.2022.3220485

I. Introduction

SPIN-TRANSFER torque magnetoresistive random access memory (STT-MRAM) has shown great potential as a replacement for SRAM cache due to its low latency [1] and for embedded Flash due to its high endurance, retention, and favorable form factor [2]. The principle behind the operation of STT-MRAM is the reversible flipping of magnetic spins in the free layer (FL) relative to magnetization in the reference layer (RL) using current density in a range of 5–7 MA/cm^2. The parallel (P) and antiparallel (AP) magnetization configurations correspond to low (R_P) and high (R_{AP}) resistance states, respectively.

Several studies on time-dependent dielectric breakdown (TDDB) in ultrathin MgO layer have shown that it can be described by the ξ-model [3], [4], [5], $1/\xi$ model [5], [6], [7], [8], [9], or the power law model [8], [9], [10], [11], with latest studies showing that the power law model is the most appropriate [12], [13]. Solutions to improve the endurance of STT-MRAM have also been studied with regard to the impact of process integration and fabrication impact, accounting for the effects of process steps such as etching, encapsulation, and annealing [9], [10], [11], [14], [15]. Further solutions to improve STT-MRAM endurance include increasing the write efficiency [16] and enhancing the thermal stability [17]. It is increasingly evident that the MgO breakdown is driven by multiple mechanisms [18], [19]. Despite the above studies conducted by various groups, the explicit role of voltage, current, and temperature in the defect generation process is still unknown.

It has been reported that self-heating has a severe impact on device endurance by accelerating breakdown [6], [9], [10]. In our study, with the use of 3-D numerical simulations, the role of self-heating and its dependence on operating conditions have been quantified. Subsequently, self-heating correction (SHC) has been appropriately done during the analysis of the stress test results.

The tunnel magnetoresistance (TMR) of industrial-grade magnetic tunnel junction (MTJ) is ~50%–100% at typical TDDB voltage conditions; as such, there is a large asymmetry in the switching current inherent to the device operation. This complicates the TDDB analysis resulting in a need to look

This work is licensed under a Creative Commons Attribution 4.0 License. For more information, see https://creativecommons.org/licenses/by/4.0/

beyond traditional MgO breakdown mechanisms reported thus far [20]. This study is aimed at understanding the breakdown mechanism by testing TDDB with different pulse voltage magnitude and polarity, device area, and temperature. We find that the differences in TDDB for the positive and negative modes are mainly caused by self-heating. The TDDB of the positive and negative modes is non-Arrhenius, unlike the Arrhenius trend for the bipolar mode. Bipolar TDDB activation energy (E_a) is shown to have a bimodal behavior. The effects of current, self-heating, charge trapping, and interface strain on MgO breakdown are discussed and a hypothesis for the breakdown model is proposed.

II. Test Structure and Electrical Characterization

The MTJ stack was deposited using magnetron sputtering on 300-mm Si wafers. FL and RL are CoFeB-based ferromagnets and the RL is pinned with synthetic antiferromagnet (SAF) layers. The MTJ devices studied were cylindrical with nominal diameters of target critical dimension (TCD), TCD −15% and TCD +15%. All three diameters were between 50 and 100 nm. Pulsed voltage TDDB tests with a 200-ns pulsewidth were used to measure MgO endurance for bit cell arrays comprising 256 devices per set for positive, negative, and bipolar modes. Positive polarity is defined as a current flow from RL to FL, as shown in Fig. 1(a). MTJ devices are set to the AP and P states for positive and negative voltages, respectively. Typical resistance–voltage (R–V) characteristics are shown in Fig. 1(b), and note that R_{AP} at high positive voltage is ∼50%–100% larger than R_P.

III. Results and Discussion

A. Calibration of STT-MRAM Device Performance

The measured resistance–hysteresis (R–H) curves to determine the current level and resistance of the devices at various voltages are shown in Fig. 1(c). Even at high bias, R_P state values remain relatively constant, while R_{AP} decreases significantly with increasing voltage. The extracted TMR = $(R_{AP}-R_P)/R_P \times 100\%$ is plotted in Fig. 1(d). The value of TMR decreases by around 60% at ±750 mV with reference to the zero-field value. Fig. 1(e) shows the R–H loop measured for $V = 10$ mV at $T = 25$ °C, 85 °C, and 125 °C. Note the reduction in TMR by 20% with increasing temperature from 25 °C to 125 °C [see Fig. 1(f)]. These TMR dependencies suggest that the extent of asymmetry in the tunneling current for different pulsing modes depends heavily on stress voltage and internal temperature, which in turn affects the TDDB lifetime of these devices and makes them sensitive to the polarity of the voltage used.

B. 3-D Self-Heating Simulation

To quantify the internal temperature rise due to self-heating, the 3-D heat-diffusion equation (1) has been solved along with the Landau–Lifshitz–Gilbert–Slonczewski (LLGS) equation [21] using the finite-element method

TABLE I
k (W · m^{-1} · K^{-1}), ρ (kg · m^{-3}), and c (J · kg^{-1} · K^{-1}) Values Used in the 3-D Self-Heating Simulation

Material	k	ρ	c
TaN	3	13800	210
MgO	48	3580	940
CoFeB	87	7700	440
Co	100	8900	420
Pt	71.6	21450	133
Cu (Electrode)	401	8940	390
SiO_2 (Encapsulation)	1.4	2320	703

$$\rho c\left(\frac{\partial T}{\partial t}\right) = k\left(\frac{\partial^2 T}{\partial x^2} + \frac{\partial^2 T}{\partial y^2} + \frac{\partial^2 T}{\partial z^2}\right) + \frac{I^2 R}{V}. \qquad (1)$$

Here, ρ (Kgm^{-3}) is the material density, c (Jkg^{-1}K^{-1}) is the specific heat capacity, and k (Wm^{-1}K^{-1}) is the thermal conductivity, with values shown in Table I. V is the volume, and I^2R is the rate of heat generation due to current I and resistance R of the MTJ. The associated current and resistance have been calculated from the dynamics of the FL of MTJ by self-consistently solving the LLGS equation. A constant voltage pulse of 0.94 V was applied for 5 μs, which was enough to reach the steady-state temperature of the device [5], [6], [10], [18], [22], [23], [24]. Within this framework, mass density, thermal conductivity, and specific heat capacity of all the layers were considered. The outer boundary of the encapsulation of the stack was kept fixed at 298 K. It may be noted that even though the encapsulation and electrode are not shown in the thermal distribution, the full device comprising electrode, stacked layers, and encapsulation were considered in the heat simulation study.

The spatial distribution of temperature [see Fig. 1(e)] of the entire STT-MRAM stack shows that the highest temperature rise is in the MgO layer. The obtained temperature rise in the MgO layer of the devices is shown in Fig. 1(f) and (g) under positive and negative stressing modes, respectively. As expected, the temperature in the MgO layer is higher by 20—50 K for the negative stressing mode due to the lower resistance of the R_P state.

To validate the self-heating simulation, ΔT_{sim} was compared with experimentally extracted internal temperature rise (ΔT_{exp}) using (2) from [22], where ΔP is the dissipated power and ϕ_{th} is the thermal resistance and is a constant fitting parameter that heavily depends on the local material stack environment surrounding the MgO layer. Note that the electrical resistance R_{MTJ} is experimentally measured and, as such, inherently considers the nonlinear changes in R_{MTJ} under different stress voltages and ambient temperature conditions. When the trends of decreasing TMR with increasing stress voltage and ambient temperature from Fig. 1(c) and (d) are accounted for, the estimates of ΔT_{exp} match very well with ΔT_{sim}, with an error of ∼1%. Note that ϕ_{th}, here, is a fitting parameter with values

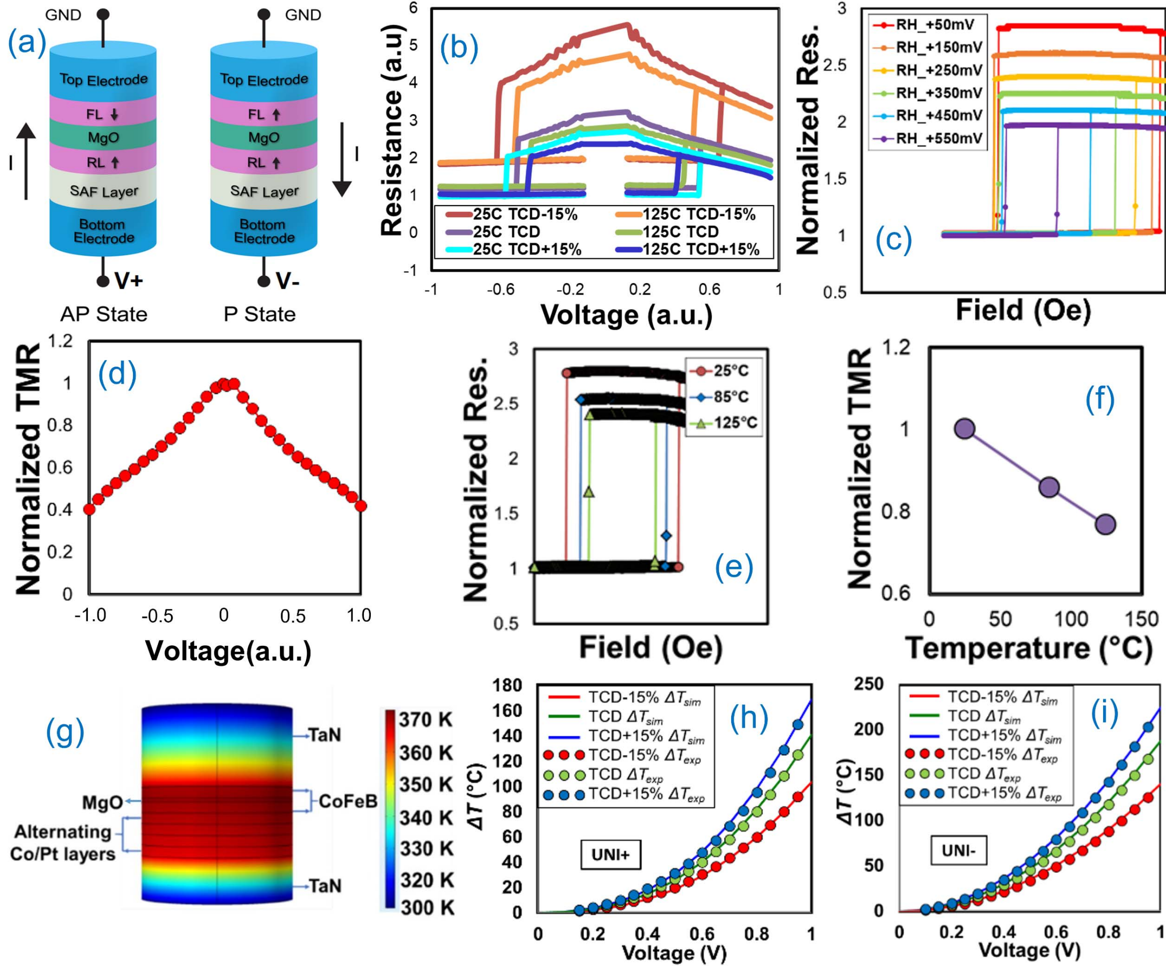

Fig. 1. (a) Simplified perpendicular MTJ structure, current direction, and voltage definition for the device in the P and AP states. (b) MTJ normalized *R*–*V* characteristics at 25 °C and 125 °C for devices with different diameters: TCD, TCD +15%, and TCD −15%. (c) *R*–*H* loops of a particular MTJ measured with different voltage biases at 25 °C. (d) Normalized TMR of device for different voltages at 25 °C, extracted from (c). (e) *R*–*H* loops of a particular MTJ measured at 25 °C–125 °C for a voltage of 10 mV. (f) Normalized TMR of device at different temperatures from 25 °C to 125 °C extracted from (e). (g) Temperature distribution of the device obtained from the numerical solution of the 3-D heat-diffusion equation shown in (1). Simulated (ΔT_{sim}) and experimentally extracted temperature increase (ΔT_{exp}) due to self-heating for different diameters of the MTJs in (h) positive mode and (i) negative mode of stressing.

TABLE II
ϕ_{TH} (°C/μW) VALUES EXTRACTED FROM FIG. 1(F) AND (G) FOR DIFFERENT DEVICE DIAMETERS

	TCD-15%	TCD	TCD+15%
Positive	0.69	0.54	0.54
Negative	0.43	0.41	0.38

shown in Table II. Smaller CD devices have higher ϕ_{th} as they have smaller cross-sectional area contacts with the top and bottom electrodes to dissipate heat. The significant deviation in positive mode ϕ_{th} is likely due to varying dependencies of R_{AP} on voltage for different device sizes

$$\Delta T_{\text{exp}} = \Delta P \cdot \phi_{\text{th}} = \frac{V_{\text{stress}}^2}{R_{\text{MTJ}}} \cdot \phi_{\text{th}}. \tag{2}$$

Considering the high current density (∼6–10 MA/cm^2) used in our accelerated cycling test, the effects of self-heating must be considered prior to quantitative comparison of the temperature-dependent breakdown data. It is to be noted that for STT-MRAM devices that even under typical operating conditions which involve tunneling current densities of ∼3–5 MA/cm^2, self-heating plays a prominent role and needs to be accounted for. This contrasts with logic and other nonvolatile memory devices where the self-heating effects under nominal operating conditions are minimal. The self-heating simulations, coupled with spintronic simulations performed in this work, provide further insight into self-heating with due consideration of switching dynamics of the MTJs.

C. TDDB Asymmetry in Positive and Negative Stress

Fig. 2(a) plots the trend of mean-time-to-failure (MTTF) versus voltage from 0.80 to 0.95 V at $T = 25$ °C–125 °C for a TCD device. The time to failure is defined as the cumulative duration of nonzero voltage pulses applied to the device until the first drop in the resistance to <50% of R_{P}. Breakdown distribution is assumed to follow the Weibull trend [9], [10], [11], [18], [19]. We observed that the negative

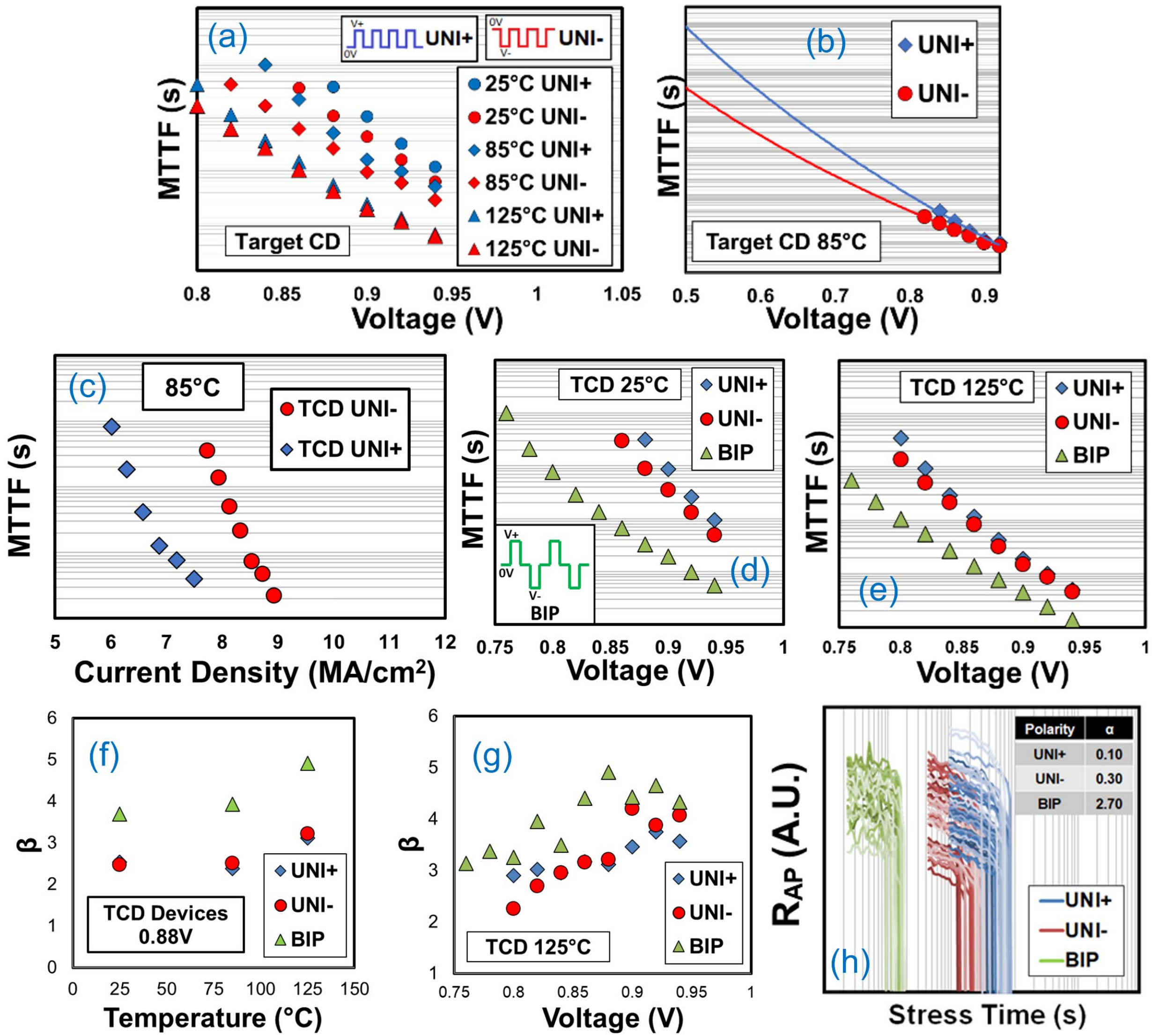

Fig. 2. (a) MTTF versus voltage stress for positive (UNI+) and negative (UNI−) modes (inset) at ambient 25 °C, 85 °C, and 125 °C for devices with a diameter of TCD. (b) Extrapolation of TDDB data using a power law model. Lifetimes for positive (UNI+) and negative (UNI−) modes can differ by three to four orders. (c) MTTF versus current density for positive (UNI+) and negative (UNI−) modes at ambient 85 °C for TCD devices. MTTF versus voltage for positive (UNI+), negative (UNI−), and symmetric bipolar (BIP) stress modes at ambient (d) 25 °C and (e) 125 °C for devices with a diameter of TCD. (f) Weibull slope (β) versus temperature for positive (UNI+), negative (UNI−), and symmetric bipolar (BIP) modes at 0.88 V for TCD diameter devices. (g) Weibull slope (β) versus applied bias for positive (UNI+), negative (UNI−), and symmetric bipolar (BIP) modes at 125 °C for devices with a diameter of TCD. (h) Trend of degradation in R_{AP} versus stress time for positive (UNI+), negative (UNI−), and bipolar (BIP) modes at ambient 25 °C for TCD diameter devices.

stress always yields a lower lifetime than that of the positive stress for any combination of voltage and temperature, and the difference in the extrapolated MTTF (using the power law extrapolation model) [12], [13] can be up to three to four orders of magnitude [see Fig. 2(b)]. Devices in the negative stress mode experience a higher current density due to low-resistance R_P state, leading to shorter MTTF. Note that the positive and negative MTTFs converge at higher temperatures and voltages due to reduced TMR.

D. TDDB Dependence on Current Density

Given the high nominal current density–low voltage operating regime of STT-MRAM, it is necessary to determine whether the breakdown is mainly current-driven. The trend of MTTF versus current density for the positive and negative modes shown in Fig. 2(c) reveals the contrary. For the same current density, the MTTF for the negative mode can be a few orders higher than the positive mode. This suggests that neither current nor voltage alone is responsible for breakdown, and both current and voltage have a collective role to play, which will be discussed later in Section III-G.

E. Lowest Lifetime for Bipolar Stress

Based on the trends above, it may be logical to assume that the bipolar mode will have an MTTF in between the positive and negative modes. However, this is not the case. As shown in Fig. 2(d) and (e), MTTF for the bipolar mode is always the lowest across all device areas, voltages, and temperatures.

This shorter lifetime for bipolar stress is discussed in further detail in the subsequent sections.

F. Weibull Slope Comparison for Different Stress Modes

As shown in Fig. 2(f) and (g), we notice that at all temperatures and voltages, the Weibull slope (β) is much higher for the bipolar mode, compared to that of both positive and negative stresses. Moreover, the value of β remains unchanged for the positive and negative modes, suggesting that they have the same mechanism of degradation. The higher value of β for the bipolar mode (β_{bipolar}) could be attributed to higher defect generation efficiency (α) according to the percolation model [25], where β and α are linearly correlated. The value of α may be empirically estimated from the downward slope of the resistance-time degradation trend during endurance tests of the devices in the bipolar mode, closer to the breakdown transient [see Fig. 2(h)]. The higher value of α_{bipolar} $\sim$2.7, compared to α_{positive} $\sim$0.1 and α_{negative} $\sim$0.3, agrees with higher β_{bipolar}. Another noteworthy trend is the consistently increasing β with stress voltage and T, again due to an enhancement in α caused by higher trap-assisted tunneling current [21] and thermal stress in the dielectric.

G. Non-Arrhenius Trend of MgO Breakdown

Fig. 3(a) shows the Arrhenius plot of MTTF in MgO for the positive, negative, and bipolar modes in a device of TCD diameter, where k_B is Boltzmann's constant. The Arrhenius plot can be corrected for self-heating by translating the Arrhenius plots along the x-axis for each mode by ΔT from Fig. 1(f) and (g), as shown in Fig. 3(b). The bipolar mode was corrected with ΔT from the negative mode as that represents the worst case scenario temperature rise under bipolar stress. After SHC, the Arrhenius plots of the positive and negative modes clearly depict the same trend, suggesting that they share the same underlying breakdown mechanism. However, the Arrhenius plot trend for the bipolar stressing still significantly deviates from both the positive and negative modes, indicating the presence of an additional mechanism that causes degradation of the MgO.

Another important observation from Fig. 3(b) is the highly non-Arrhenius behavior for the positive and negative modes of stressing, while the bipolar data show a clear Arrhenius trend. The non-Arrhenius behavior of the positive and negative modes could be due to the unidirectional stressing and charge trapping [4], [26] as well as the complex non-Arrhenius dependence of charge transport mechanisms such as inelastic trap-assisted tunneling. As for the bipolar mode of stressing, the convoluted effect of multiple possible phenomena, including charge trapping at both interfaces, mechanical strain induced by compressive-tensile strain changes in the MgO–CoFeB interface, as well as voltage, current, and temperature results in a "pseudo-Arrhenius" trend. Based on the model proposed by Wu et al. [27] for SiO_2 and HfO_2 which also display non-Arrhenius dependence of time-to-breakdown, the generation of oxygen vacancies at the MgO–CoFeB interface through Mg–O bond breaking via multiple electron-induced coherent vibrational excitations could be the origin for the non-Arrhenius trend for the positive and negative modes.

The bipolar mode TDDB E_a with and without SHC is plotted with voltage in Fig. 3(c). It is clearly seen that E_a decreases with voltage and has a bimodal behavior with different sensitivity to voltage. Similar E_a trends have been reported in SiO_2 dielectrics [28], [29], [30], [31], but there has been no clear explanation provided to the best of our knowledge. Considering the conducting nature of 1-nm MgO-based STT-MRAM devices, there could be multiple combined effects contributing to the E_a trend such as current, self-heating, charge trapping [4], [26], and interface strain along with the voltage effect. Noman et al. [32] reported electron trapping-induced filament formation in TiO_2-based resistive devices contributing to percolation path formation. With the large applied current density in our MgO devices, electron trapping could take place at preexisting oxygen vacancies, the presence of boron oxide or lattice mismatches at the CoFeB–MgO interface [4], [21] that can lead to strong localized fields. The trapped electrons result in greater current flow in the local region, which further induces more electron trapping. This process speeds up to create structural changes that lead to the formation of a breakdown percolation path when the localized field, current, and temperature reach a threshold value. The bimodal trend of E_a could also be driven by the formation of defects [33] and/or voltage-induced CoFeB–MgO interface strain [34] through the breaking of Mg–O bonds. In addition, the bimodal trend of E_a could be due to multiple breakdown pathways as reported in [30] and [35].

H. Power Law Model for MgO Breakdown

The power law model has been proposed by Wu et al. [36] to describe breakdown processes that are both field and current-driven. The power exponent from the power law model fitting [see Fig. 3(d)] is represented as a function of temperature in Fig. 3(e). The monotonic reduction in the power exponent with temperature for all three stress modes is an additional confirmation of the validity of the power law, which is recommended for current and field co-induced breakdown [37]. The power exponent trend against temperature is a signature of the physical breakdown mechanism. Referring to Fig. 3(e), after SHC, the positive and negative modes' power exponent trends match well as indicated by the dotted line, hence implying that they share the same signature. However, the bipolar power exponent trend deviates significantly from the other two modes after SHC, which indicates a different breakdown mechanism. These suggest that the main difference between the positive and negative breakdown is due to self-heating, while the bipolar breakdown is driven by a fundamentally different process.

I. Physical Mechanism of MgO Breakdown

We propose a schematic illustrating the breakdown mechanism as shown in Fig. 3(f) with "U" denoting the defects of the unipolar positive and negative modes and "B" denoting the bipolar modes defects. It is evident that breakdown cannot

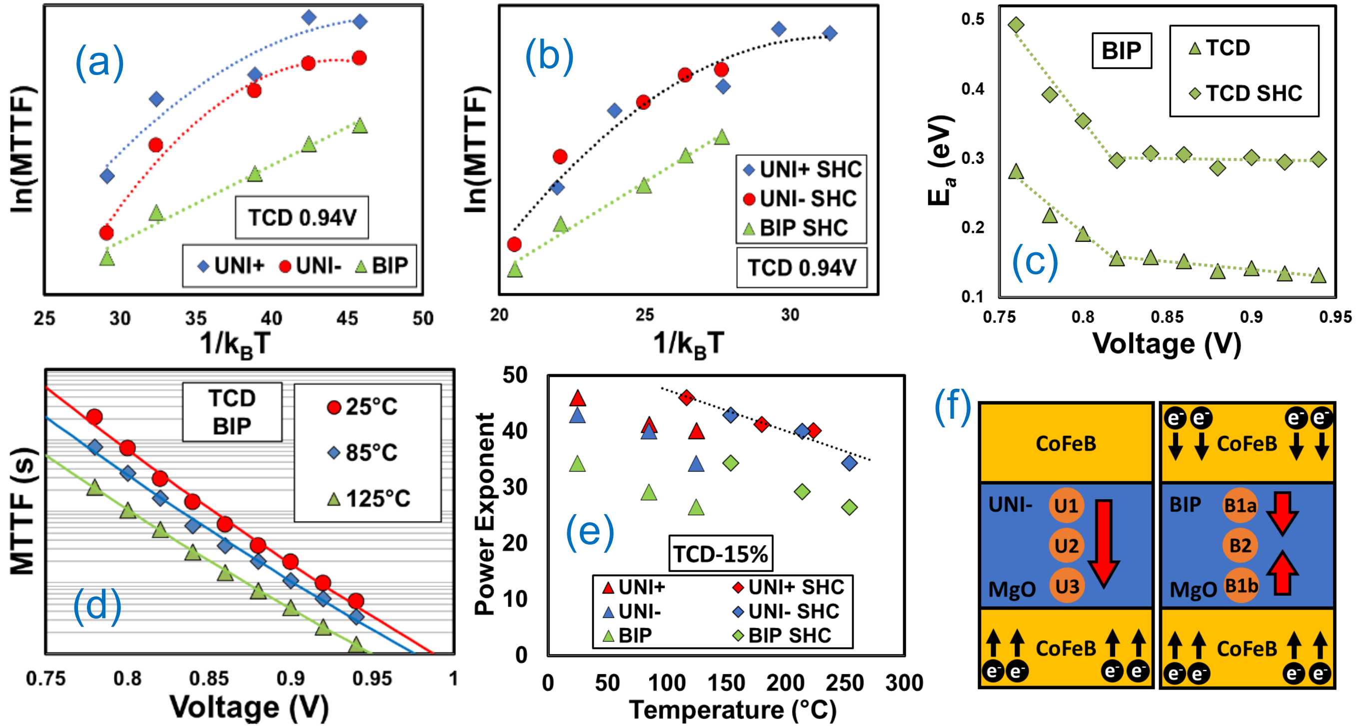

Fig. 3. Arrhenius plot (a) as measured and (b) with SHC for positive (UNI+), negative (UNI−), and bipolar (BIP) modes at 0.94 V with temperatures −20 °C, 0 °C, 25 °C, 85 °C, and 125 °C for TCD diameter devices. Dotted lines are designed for visual aid. (c) Activation energies at different voltage stress under bipolar (BIP) stress as measured and with SHC for devices with a diameter of TCD. Dotted lines are designed for visual aid. (d) MTTF versus voltage stress for symmetric bipolar (BIP) mode at 25 °C–125 °C with the corresponding power law fit for devices with a diameter of TCD. (e) Trend of power-law exponent versus temperature for positive (UNI+), negative (UNI−), and bipolar (BIP) modes with and without SHC for TCD −15% diameter devices. (f) Sequence of defect generation in the MTJ for positive, negative, and bipolar modes. The numbers inside the circles represent order of locations where defects are generated. "1a" and "1b" imply equally probable locations for the first defect to be generated. The red arrows denote the directional evolution of percolation.

be described by "current only" or "voltage only." The field-free Mg–O bond energy of 2.0–4.4 eV as obtained from experimental and DFT studies [18], [20], [22], [38], [39] is significantly higher than the maximum ballistic electron energy of 0.94 eV. The breakdown process in the 1-nm MgO layer could proceed in two stages: 1) current-assisted defect generation at the interface and 2) field-assisted defect generation in the bulk.

In the positive and negative modes, the first defect is generated at the MgO–CoFeB anode interface through multiple electron-induced coherent vibrational excitations of the Mg–O bond due to trapped charges and high charge fluence (U1). These interfacial defects reduce E_a for bulk defects to be created in their vicinity (U2). The bulk defects trigger the final defect (U3) at the other MgO–CoFeB interface to be generated in its vicinity, again due to lower E_a caused by lattice relaxation.

In the bipolar mode, both MgO–CoFeB interfaces are equally susceptible to nucleate the percolation path. Charge trapping and defect generation probability are high at both interfaces (B1a/B1b). The trapped charges and/or nucleation of defects at both interfaces drastically reduce E_a for MgO bulk defect generation (B2) resulting in easier percolation. Hence, MTTF for the bipolar mode is much smaller than that of the unipolar modes. Considering that 1-nm MgO is 4–6 monolayer thick, it is expected that the percolation path comprises only around three defects.

IV. Conclusion

A holistic comparison of TDDB lifetime trends in STT-MRAM devices is presented considering three different types of pulse stressing modes and SHC with varying device area and temperature. After SHC, it was shown that positive and negative modes have similar TDDB trends, implying that they share the same breakdown mechanism. The bipolar TDDB trends deviate significantly. Bipolar TDDB E_a versus stress voltage trend was observed to have a bimodal behavior that could be due to charge trapping, interface strain, or model mixing. Our results support a degradation model driven by both current and field, leading to a fluence-field co-assisted breakdown mechanism, which complicates the physics of failure for the commonly used bipolar pulse condition. Analysis of Mg–O breakdown via atomic force microscopy or in situ transmission electron microscopy could reveal more insights into the structural changes and strain effects. Further density functional theory calculations of the defect energetics, charge trapping, and breakdown transients are required to unveil the fundamental physics of breakdown in ultrathin MgO stacks.

Acknowledgment

The authors would like to acknowledge Everspin Technologies,[1] Chandler, AZ, USA, for their technical expertise in the fabrication of the devices used in this work.

[1] Registered trademark.

References

[1] T. Y. Lee et al., "Advanced MTJ stack engineering of STT-MRAM to realize high speed applications," in *IEDM Tech. Dig.*, Dec. 2020, p. 11, doi: 10.1109/IEDM13553.2020.9372015.

[2] V. B. Naik et al., "STT-MRAM: A robust embedded non-volatile memory with superior reliability and immunity to external magnetic field and RF sources," in *Proc. Symp. VLSI Technol.*, 2021, pp. 1–2.

[3] Y. Wang et al., "Compact model of dielectric breakdown in spin-transfer torque magnetic tunnel junction," *IEEE Trans. Electron Devices*, vol. 63, no. 4, pp. 1762–1767, Apr. 2016, doi: 10.1109/TED.2016.2533438.

[4] S. Amara-Dababi et al., "Charge trapping-detrapping mechanism of barrier breakdown in MgO magnetic tunnel junctions," *Appl. Phys. Lett.*, vol. 99, May 2011, Art. no. 083501, doi: 10.1063/1.3615654.

[5] C.-M. Choi et al., "Temperature dependence of reliability characteristics for magnetic tunnel junctions with a thin MgO dielectric film," *Semiconductor Sci. Technol.*, vol. 31, no. 7, 2016, Art. no. 075004, doi: 10.1088/0268-1242/31/7/075004.

[6] X. Zhang, G. Zhang, L. Shen, P. Yu, and Y. Jiang, "Life-time degradation of STT-MRAM by self-heating effect with TDDB model," *Solid-State Electron.*, vol. 173, Nov. 2020, Art. no. 107878, doi: 10.1016/j.sse.2020.107878.

[7] J. J. Kan et al., "Systematic validation of 2X nm diameter perpendicular MTJ arrays and MgO barrier for sub-10 nm embedded STT-MRAM with practically unlimited endurance," in *IEDM Tech. Dig.*, Dec. 2016, p. 27, doi: 10.1109/IEDM.2016.7838493.

[8] C.-M. Choi, H. Sukegawa, S. Mitani, and Y.-H. Song, "TDDB modeling depending on interfacial conditions in magnetic tunnel junctions," *Semiconductor Sci. Technol.*, vol. 32, no. 10, Oct. 2017, Art. no. 105007, doi: 10.1088/1361-6641/aa856e.

[9] S. Van Beek, B. J. O'Sullivan, S. Couet, D. Crotti, D. Linten, and G. S. Kar, "Understanding and empirical fitting the breakdown of MgO in end-of-line annealed MTJs," in *Proc. IEEE Int. Rel. Phys. Symp. (IRPS)*, Apr. 2020, pp. 1–5, doi: 10.1109/IRPS45951.2020.9129551.

[10] S. Van Beek et al., "Impact of self-heating on reliability predictions in STT-MRAM," in *IEDM Tech. Dig.*, Dec. 2018, p. 25, doi: 10.1109/IEDM.2018.8614617.

[11] S. Van Beek et al., "Study of breakdown in STT-MRAM using ramped voltage stress and all-in-one maximum likelihood fit," in *Proc. 48th Eur. Solid-State Device Res. Conf. (ESSDERC)*, Sep. 2018, pp. 146–149, doi: 10.1109/ESSDERC.2018.8486879.

[12] K. Suh et al., "12.5 Mb/mm^2 embedded MRAM for high density non-volatile RAM applications," in *Proc. Symp. VLSI Technol.*, 2021, pp. 1–2.

[13] V. B. Naik et al., "A reliable TDDB lifetime projection model verified using 40 Mb STT-MRAM macro at sub-ppm failure rate to realize unlimited endurance for cache applications," in *Proc. IEEE Symp. VLSI Technol.*, Jun. 2020, pp. 1–2, doi: 10.1109/VLSITechnology18217.2020.9265086.

[14] S. Van Beek et al., "Impact of processing and stack optimization on the reliability of perpendicular STT-MRAM," in *Proc. IEEE Int. Rel. Phys. Symp. (IRPS)*, Apr. 2017, pp. 1–5, doi: 10.1109/IRPS.2017.7936318.

[15] S. Van Beek et al., "Edge-induced reliability & performance degradation in STT-MRAM: An etch engineering solution," in *Proc. IEEE Int. Rel. Phys. Symp. (IRPS)*, Mar. 2021, pp. 1–5, doi: 10.1109/IRPS46558.2021.9405209.

[16] S. Miura et al., "Scalability of quad interface p-MTJ for 1X nm STT-MRAM with 10-ns low power write operation, 10 years retention and endurance $> 10^{11}$," *IEEE Trans. Electron Devices*, vol. 67, no. 12, pp. 5368–5373, Dec. 2020, doi: 10.1109/TED.2020.3025749.

[17] G. Wang et al., "Compact modeling of perpendicular-magnetic-anisotropy double-barrier magnetic tunnel junction with enhanced thermal stability recording structure," *IEEE Trans. Electron Devices*, vol. 66, no. 5, pp. 2431–2436, May 2019, doi: 10.1109/TED.2019.2906932.

[18] J. H. Lim et al., "Investigating the statistical-physical nature of MgO dielectric breakdown in STT-MRAM at different operating conditions," in *IEDM Tech. Dig.*, Dec. 2018, p. 25, doi: 10.1109/IEDM.2018.8614515.

[19] J. H. Lim et al., "Asymmetric dielectric breakdown behavior in MgO based magnetic tunnel junctions," *Microelectronic Eng.*, vol. 178, pp. 308–312, Jun. 2017, doi: 10.1016/j.mee.2017.05.033.

[20] J. H. Lim et al., "Correct extrapolation model for TDDB of STT-MRAM MgO magnetic tunnel junctions," in *Proc. IEEE Int. Rel. Phys. Symp. (IRPS)*, Mar. 2019, pp. 1–7, doi: 10.1109/IRPS.2019.8720611.

[21] B. Sikder et al., "Analysis and simulation of interface quality and defect induced variability in MgO spin-transfer torque magnetic RAMs," *IEEE Electron Device Lett.*, vol. 42, no. 1, pp. 34–37, Jan. 2021, doi: 10.1109/LED.2020.3040131.

[22] S. Van Beek, "Reliability characterization of STT-MRAM magnetic memory. The impact of self-heating," KU Leuven, Leuven, Belgium, Tech. Rep. lirias1988601, 2018, ch. 3, p. 30. [Online]. Available: https://lirias.kuleuven.be/retrieve/515586

[23] R. C. Sousa et al., "Crossover in heating regimes of thermally assisted magnetic memories," *J. Appl. Phys.*, vol. 99, no. 8, Apr. 2006, Art. no. 08N904, doi: 10.1063/1.2165581.

[24] K. Hosotani et al., "Effect of self-heating on time-dependent dielectric breakdown in ultrathin MgO magnetic tunnel junctions for spin torque transfer switching magnetic random access memory," *Jpn. J. Appl. Phys.*, vol. 49, no. 4S, Apr. 2010, Art. no. 04DD15, doi: 10.1143/JJAP.49.04DD15.

[25] J. Suñé, E. Y. Wu, and S. Tous, "A physics-based deconstruction of the percolation model of oxide breakdown," *Microelectronic Eng.*, vol. 84, nos. 9–10, pp. 1917–1920, Sep. 2007, doi: 10.1016/j.mee.2007.04.008.

[26] A. Padovani, D. Z. Gao, A. L. Shluger, and L. Larcher, "A microscopic mechanism of dielectric breakdown in SiO_2 films: An insight from multi-scale modeling," *J. Appl. Phys.*, vol. 121, no. 15, Apr. 2017, Art. no. 155101.

[27] E. Wu, J. Suñé, C. Larow, and R. Dufresne, "Temperature dependence of TDDB voltage acceleration in high-K/SiO_2 bilayers and SiO_2 gate dielectrics," in *IEDM Tech. Dig.*, Dec. 2012, p. 28, doi: 10.1109/IEDM.2012.6479123.

[28] J. Prendergast, J. Suehle, P. Chaparala, E. Murphy, and M. Stephenson, "TDDB characterisation of thin SiO_2 films with bimodal failure populations," in *Proc. 33rd IEEE Int. Rel. Phys. Symp.*, Apr. 1995, pp. 124–130, doi: 10.1109/RELPHY.1995.513665.

[29] W. M. Miller, N. F. Smith, C. Messick, and J. A. Shideler, "Evidence for a correct SiO_2 voltage acceleration model," in *Proc. Int. Integr. Rel. Workshop*, 1993, pp. 45–51.

[30] A. Shanware, R. B. Khamankar, and W. McPherson, "Resolving the non-uniqueness of the activation energy associated with TDDB for SiO_2 thin films," in *IEDM Tech. Dig.*, Dec. 2000, pp. 549–552, doi: 10.1109/IEDM.2000.904378.

[31] R.-P. Vollertsen and W. W. Abadeer, "Upper voltage and temperature limitations of stress conditions for relevant dielectric breakdown projections," *Qual. Rel. Int.*, vol. 11, no. 4, pp. 233–238, 1995, doi: 10.1002/qre.4680110404.

[32] M. Noman et al., "Mechanism of localized electrical conduction at the onset of electroforming in TiO_2 based resistive switching devices," *Appl. Phys. Lett.*, vol. 104, no. 11, Mar. 2014, Art. no. 113510, doi: 10.1063/1.4869230.

[33] S. Choudhury, D. Morgan, and B. P. Uberuaga, "Massive interfacial reconstruction at misfit dislocations in metal/oxide interfaces," *Sci. Rep.*, vol. 4, no. 1, May 2015, doi: 10.1038/srep06533.

[34] V. B. Naik et al., "Effect of electric-field on the perpendicular magnetic anisotropy and strain properties in CoFeB/MgO magnetic tunnel junctions," *Appl. Phys. Lett.*, vol. 105, no. 5, 2014, Art. no. 052403, doi: 10.1063/1.4892410.

[35] J. W. McPherson, R. B. Khamankar, and A. Shanware, "Complementary model for intrinsic time-dependent dielectric breakdown in SiO_2 dielectrics," *J. Appl. Phys.*, vol. 88, no. 9, pp. 5351–5359, Nov. 2000, doi: 10.1063/1.1318369.

[36] E. Y. Wu, "Facts and myths of dielectric breakdown processes—Part I: Statistics, experimental, and physical acceleration models," *IEEE Trans. Electron Devices*, vol. 66, no. 11, pp. 4523–4534, Nov. 2019, doi: 10.1109/TED.2019.2933612.

[37] G. Ribes et al., "Multi-vibrational hydrogen release: Physical origin of TBD, QBD power-law voltage dependence of oxide breakdown in ultra-thin gate oxides," *Microelectron. Rel.*, vol. 45, no. 12, pp. 1842–1854, Dec. 2005, doi: 10.1016/j.microrel.2005.03.009.

[38] A.-M. El-Sayed, M. B. Watkins, T. Grasser, and A. L. Shluger, "Effect of electric field on migration of defects in oxides: Vacancies and interstitials in bulk MgO," *Phys. Rev. B, Condens. Matter*, vol. 98, no. 6, Aug. 2018, doi: 10.1103/PhysRevB.98.064102.

[39] K. P. McKenna and A. L. Shluger, "First-principles calculations of defects near a grain boundary in MgO," *Phys. Rev. B*, vol. 79, no. 22, Jun. 2009, doi: 10.1103/PhysRevB.79.224116.